Check for updates

ChemElectroChem

Research Article
doi.org/10.1002/celc.202300673

Chemistry Europe
European Chemical Societies Publishing

www.chemelectrochem.org

Highly Active MoS_2-MXenes Hybrid Electrocatalysts Towards the Oxygen Reduction Reaction

Yapci Remedios-Díaz,[a] Stefan Delgado,[a] Juan Carlos Calderón,*[a] Laura Calvillo,[b] María del Carmen Arévalo,[a] and Elena Pastor*[a]

Dedicated to Prof. Flavio Maran for his 70th birthday

In this work, catalytic performance of MoS_2 supported on Mo_2TiC_2 and Ti_3C_2 MXenes towards the oxygen reduction reaction (ORR) was studied. These materials were synthesised through an etching route of MAX phases as precursors of MXenes, followed by a hydrothermal treatment to coat them with MoS_2. This procedure generated MoS_2 nanospheres covering the MXenes, which were verified by SEM-EDX mapping, Raman spectroscopy and XPS. Activity of these materials towards ORR was studied by RRDE, comparing its performance with that of individual MoS_2 and MXenes. As main features, it was demonstrated that production of HOO^- occurring on the composites decreases in comparison with individual materials. Long-term stability tests performed in O_2-saturated electrolyte showed a drop in the activity of the materials due to the increase in the production of HOO^-, although no morphological or compositional changes were observed. Despite this result, the improvement of the catalytic properties of the individual materials means that these composites can be considered as candidates to be used as supports of active non-noble metal nanoparticles in the cathodes of anion exchange membrane fuel cells (AEMFCs).

Introduction

Anion exchange membrane fuel cells (AEMFCs) are devices able to produce electricity from the combination of environmentally friendly fuels and oxygen. They require the use of catalytic anodes and cathodes to address the oxidation of the fuel and the reduction of the supplied oxygen, respectively.[1] If Pt-based cathodes are employed to perform the oxygen reduction reaction (ORR), oxygen dissociation after previous adsorption is promoted but this process is decelerated due to the stable Pt–O binding, thus resulting in a sluggish kinetics and the formation of oxide/hydroxide species occupying active sites on Pt.[2,3] Furthermore, it is well-known that ORR follows mechanistic pathways involving two electrons transfer with the generation of corrosive hydrogen peroxide, or four electrons for the formation of water.[4] In this sense, design of novel catalysts with outstanding activity towards ORR favouring the four electron mechanism, has capital importance to boost the implementation of AEMFCs in an environmentally friendly scheme of electricity production.

With the aim to replace noble metals from the cathodes of AEMFCs avoiding a detriment in the catalytic performance, noble metal-free catalysts with 2D structure have been designed and proposed as suitable cathodes for these devices in the last years.[5,6] The advantages attributed to this family of materials are associated to its great and hydrophilic surface area, its structure facilitating the diffusion of the electroactive species and the adequate conductivity.[7] Among these materials, MXenes appear as crystalline and multifunctional carbides or nitrides constituted by layers stacked *via* hydrogen bond and van der Waal's interactions.[8,9] The composition of these materials has been previously described as $M_{n+1}X_nT_x$, being M a transition metal (Mo, Ti, Zr, Nb, or V), X is carbon or nitrogen and T is the surface termination group (–F or –OH).[9] MXenes can be synthesised from MAX phases constituted by a transition metal and a 13–14 group element, following the formula $M_{n+1}AX_n$ (A = Al, Ga, In, Si or Pb). Chemical etching by hydrofluoric acid or fluorides in acidic media is the most common method to prepare layered MXenes.[10,11]

In previous works, it has been shown that MXenes display low performance in terms of ORR reduction currents, and promote the 2-electrons mechanism with the formation of hydrogen peroxide.[12–14] Only remarkable results for the ORR were obtained with single layers of 2D Ti_3C_2 prepared by using big size cations during the synthesis to promote the MXenes delamination.[7] In general, the low activity, together with their

[a] Y. Remedios-Díaz, S. Delgado, Dr. J. C. Calderón, Prof. M. d. C. Arévalo, Prof. E. Pastor
Instituto de Materiales y Nanotecnología, Departamento de Química
Universidad de La Laguna
AP 456, 38206, La Laguna, Santa Cruz de Tenerife, España
E-mail: jcaldero@ull.edu.es
epastor@ull.edu.es

[b] Prof. L. Calvillo
Department of Chemical Sciences, INSTM Unit
University of Padova
35131 Padova, Italy

Supporting information for this article is available on the WWW under https://doi.org/10.1002/celc.202300673

© 2024 The Authors. ChemElectroChem published by Wiley-VCH GmbH. This is an open access article under the terms of the Creative Commons Attribution License, which permits use, distribution and reproduction in any medium, provided the original work is properly cited.

© 2024 The Authors. ChemElectroChem published by Wiley-VCH GmbH

corrosion and mechanical resistance,[15] are the reasons why, to date, MXenes have been primarily considered as supports for metal nanoparticles to address the ORR. Pt, Fe and Cu nanoparticles supported on Ti MXenes are the most studied materials displaying high performances toward this reaction.[12,15,16] These works suggest that searching of modified MXenes is mandatory to obtain materials with improved catalytic activity towards ORR.

Accordingly, attempts have been made to prepare active composites based on MXenes,[17–23] especially those based on Ti. Thus, Li and co-workers deposited an iron-phthalocyanine (FePc) complex on a $Ti_3C_2T_x$ MXene by a facile mixing procedure in dimethylformamide (DMF).[18] This material induces a shift in the ORR onset potential toward positive values in comparison with the values obtained for FePc and $Ti_3C_2T_x$ acting as individual catalysts. Interactions between FePc and $Ti_3C_2T_x$ were stated by the authors as the main reason for the increase in the catalytic activity.[18] Also, it was proposed that the decrease in the work function and delocalisation of electrons promoted by the deposition of these molecules, generating new electronic distributions, contribute to the overlapping between Fe 3d and O_2 2p orbitals, thus favouring the electron transfer and the ORR kinetics.[19] Alternatively, cobalt nanoparticles encapsulated by carbon nanotubes (CNTs) and supported on $Ti_3C_2T_x$ also exhibited similar activity towards ORR to that of a Pt/C catalyst, a fact explained from the improved diffusion of the electroactive species towards the active Co nanoparticle centre of the composite and the favoured interfacial interaction between $Ti_3C_2T_x$ and the Co-CNTs complex.[20]

Taking the above into account, in the present work Ti-based MXenes composites with MoS_2 were prepared to obtain materials with improved properties as catalysts for ORR. MoS_2 has been employed as catalyst for hydrogen evolution reaction,[21,22] oxygen evolution reaction[23,24] and other applications,[25–27] but its combination with MXenes as ORR catalysts was evaluated in only a few works. MoS_2 quantum dots (QDs) supported on Ti_3C_2 have been synthesised by Yang et al.[28] and supported on multiwalled carbon nanotubes with the purpose to disperse the composite and increase the number of active sites in the material. Onset potentials around 0.85 V_{RHE} and current densities between 3 and 4 mA cm^{-2} were found, with the amount of MoS_2 quantum dots playing a key role in the performance of the composites. On the other hand, some papers reported the activity of MoS_2 towards the ORR. Arunchander and co-workers supported MoS_2 with a flower-like nanostructure on graphene materials, followed by an annealing treatment at temperatures between 400 and 600 °C. The authors have found that annealing temperature plays an important role in the electrochemical response of the catalyst, achieving the best results with the material treated at 500 °C.[29] Finally, the effect of doping was considered in the work of Tang et al.,[30] evaluating N-doped MoS_2, also supported on graphene. In this case, the combination with graphene and the presence of N as dopant element in the structure of MoS_2 were considered as the factors promoting its highest catalytic activity.[30]

Summarising, the study performed in this work focussed on the electrochemical features of MoS_2 supported on Ti-based MXenes (Mo_2TiC_2 and Ti_3C_2) when they are used as ORR catalysts. The purpose is to improve the catalytic properties of the MXenes in the composite to be used in the future as supports of non-noble metal nanoparticles as in ref.[18–20] Physicochemical and electrocatalytic properties were correlated and the stability of the materials was established to evaluate the possibilities of application of these composites in AEMFCs.

Results and Discussion

Physicochemical characterisation

Table 1 shows the atomic compositions of the different catalysts obtained from EDX analysis, confirming the absence of Al in the MXene phases and the suitability of the applied synthesis route to eliminate this metal from the MAX phases. Regarding the composition of MoS_2, an atomic ratio Mo:S around 1:2 was obtained, also ratifying the suitability of the employed synthesis method.

Figure 1 shows the morphology of the hybrid materials and MoS_2 (SEM images). The morphology of the MXene supports was already reported in a previous work.[9] According to the electron images, MoS_2 typically developed nanospheres with different size,[27] which is maintained when it is grown on the MXenes' surface. Mo, S and Ti EDX mapping images show that MoS_2 nanospheres cover the surface of Mo_2TiC_2 and Ti_3C_2 MXenes, although there are regions (marked with yellow arrows in Figure 1 a and b) where the 2D laminar structure of MXenes can be distinguished.

XRD patterns were obtained to identify the crystalline features of the MXenes, MAX phases and composites with MoS_2 (Figure 2). MAX phases display the (002) plane at 9.5° 2θ, characteristic of this type of materials. After the chemical etching to form the MXenes phases, a shift in this peak towards 7° 2θ was observed.[31] This shift has been explained from the increase in the interlayer spaces located between the MXenes

Table 1. EDX analysis of synthesised materials.

Material	Composition (at. %)							Mo:S ratio
	C	O	F	Al	Mo	Ti	S	
MoS_2	–	10.2	–	–	29.0	–	60.8	1:2.1
MoS_2@Ti_3C_2	36.2	9.3	–	–	16.4	3.5	34.6	1:2.1
MoS_2@Mo_2TiC_2	37.3	7.4	–	–	18.7	0.8	35.8	1:1.9

© 2024 The Authors. ChemElectroChem published by Wiley-VCH GmbH

21960216, 2024, 6, Downloaded from https://chemistry-europe.onlinelibrary.wiley.com/doi/10.1002/celc.202300673 by University Of Padova Center Di, Wiley Online Library on [04/02/2025]. See the Terms and Conditions (https://onlinelibrary.wiley.com/terms-and-conditions) on Wiley Online Library for rules of use; OA articles are governed by the applicable Creative Commons License

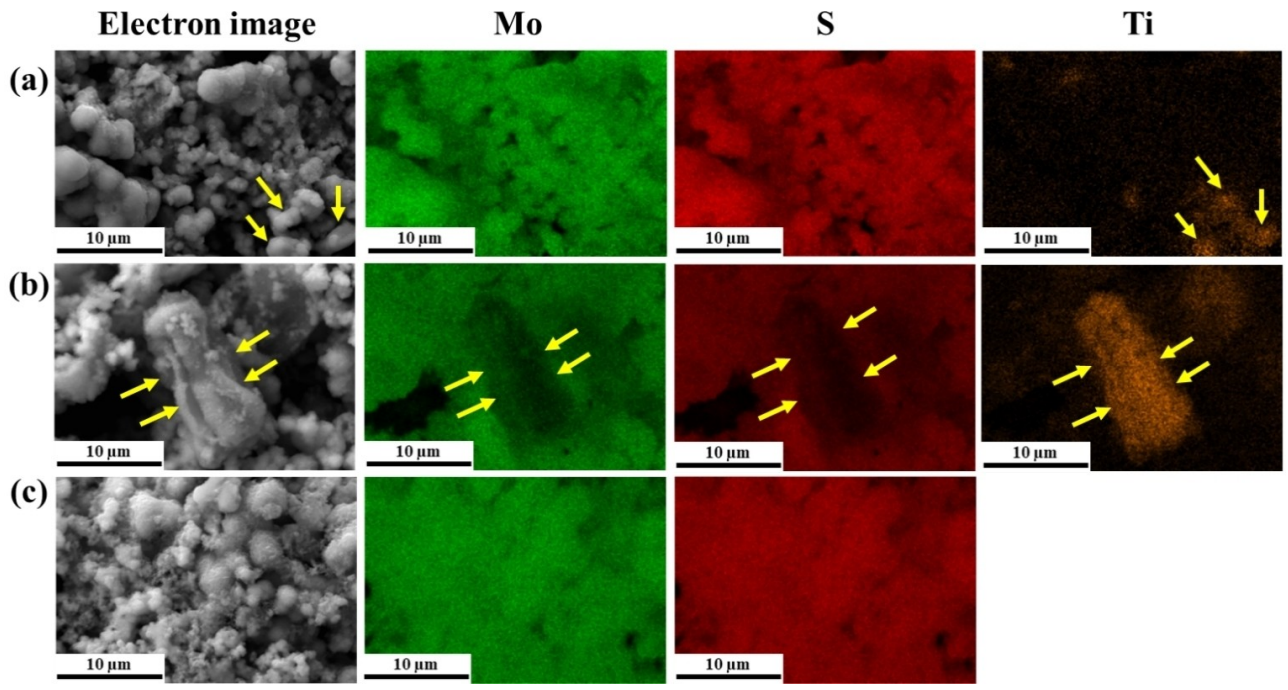

Figure 1. SEM and EDX mapping images of (a) MoS_2@Mo_2TiC_2, (b) MoS_2@Ti_3C_2 and (c) MoS_2. Yellow arrows mark the zones where MXenes are not covered with MoS_2.

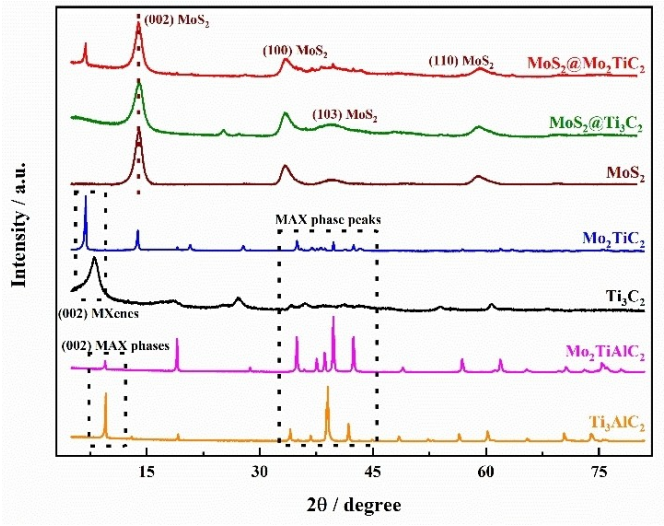

Figure 2. XRD patterns of MAX, MXenes, MoS_2 and composites.

layers after the insertion of water molecules in these spaces, previously occupied by Al.[31,32]

Other evidence of the successful Al elimination from MAX phase is the drastic decrease in the intensity of the signals located between 35 and 43° 2θ for MXene materials, as reported in previous works.[10,33,34] MoS_2@MXene composites show peaks at 14°, 33.5°, 39.5° and 59.2°, attributed to the (002), (100), (103) and (110) reflections of hexagonal 2H-MoS_2.[35,36] MoS_2@Mo_2TiC_2 also shows the peaks related to Mo_2TiC_2 with low intensity, while in the MoS_2@Ti_3C_2 patter, the peaks associated with Ti_3C_2 are not observed. These results confirm the coverage of the MXene supports by MoS_2, as seen by SEM. The (002) peak was used to calculate the crystalline parameters of MAX phases, MXenes, composites and MoS_2, and the results are reported in Table 2.

The increase in the interplanar distance, caused by the etching treatment of MAX phases to form MXenes, is explained from the insertion of water molecules between the MXenes layers, verifying the elimination of Al present in the MAX phases.[31,32] In addition, crystallite size of MXenes decreased after etching, as previously reported.[37] In the case of the catalysts containing MoS_2, similar sizes (6–8 nm) were found for MoS_2 crystallites, indicating that MXenes do not affect its structure. A similar trend was observed for the interplanar distance, exhibiting values around 0.63 nm for MoS_2, MoS_2@Mo_2TiC_2 and MoS_2@Ti_3C_2, matching with the results reported for other MoS_2 composites.[38,39]

The presence of metal oxides in the studied materials was verified by Raman spectroscopy (Figure 3). In Mo-containing

Table 2. Crystallographic parameters of the studied materials.

Catalyst	Crystallite size (002) /nm	Interplanar distance /nm
Ti_3AlC_2	79.6	0.92
Mo_2TiAlC_2	71.5	0.93
Ti_3C_2	5.8	1.10
Mo_2TiC_2	44.7	1.28
MoS_2	7.2*	0.63
MoS_2@Ti_3C_2	6.0*	0.63
MoS_2@Mo_2TiC_2	8.0*	0.64

*Corresponding to the MoS_2 peak.

© 2024 The Authors. ChemElectroChem published by Wiley-VCH GmbH

21960216, 2024, 6, Downloaded from https://chemistry-europe.onlinelibrary.wiley.com/doi/10.1002/celc.202300673 by University Of Padova Center Di, Wiley Online Library on [04/02/2025]. See the Terms and Conditions (https://onlinelibrary.wiley.com/terms-and-conditions) on Wiley Online Library for rules of use; OA articles are governed by the applicable Creative Commons License

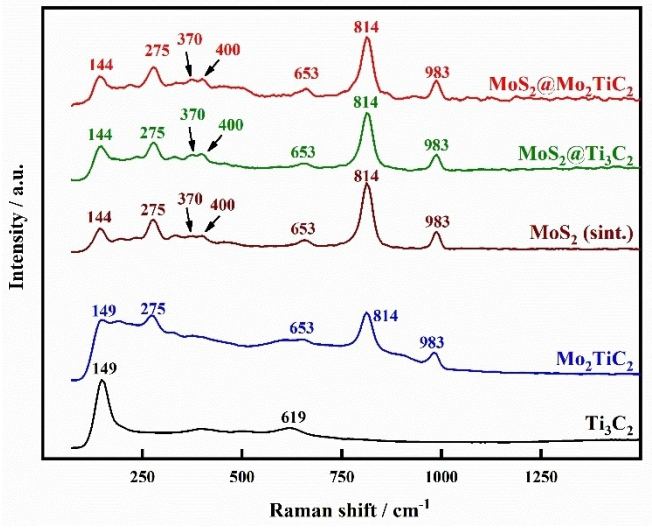

Figure 3. Raman spectra of MoS_2@MXenes, MoS_2 and MXenes.

materials, signals attributed to the lattice mode, O=Mo bending, as well as O–Mo_3, O–Mo_2 and O=Mo stretching modes, were observed at 144–149, 275, 653, 814 and 983 cm^{-1}, respectively.[40] Furthermore, the materials containing MoS_2 have developed the typical signals at 370 and 400 cm^{-1}, assigned to the in-plane E_{2g} and out-of-plane A_{1g} modes of MoS_2.[35,39] It is important to highlight that the signal associated to the lattice mode in the composites and pure sulphide appears at 144 cm^{-1} with an enhanced definition and sharpness, indicating that this signal is provided exclusively by MoS_2. Sharp signals for the lattice mode of MoS_2 has been already reported by Zhang and co-workers, who studied the formation of transition metal disulfides with layered structures by Raman spectroscopy.[41] Additionally, the Ti_3C_2 spectrum exhibited peaks associated to different O–Ti vibrational modes from TiO_2 as follows: B_{1g} at 149 cm^{-1} and A_{1g} at 619 cm^{-1}.[42–44] All information about assignation and vibration modes for all studied catalysts is reported in Table 3.

XPS analysis was conducted to identify the surface species present in the studied materials. Figure SI1 shows the survey spectra of the three materials. Only the S 2p, Mo 3d and O 1s

Table 3. Vibrational modes assignment for MXenes, MoS_2 and MoS_2@MXenes from spectra in Figure 3.

Sample	Raman shift / cm^{-1}	Assignation	Vibration mode	Ref.
Ti_3C_2	149	O–Ti	B_{1g} (TiO_2)	[10]
	619	O–Ti	A_{1g}(TiO_2)	[10]
Mo_2TiC_2	149	Lattice mode	–	[9]
	275	O=Mo	Bending	[9]
	653	O–Mo_3	Stretching	[9]
	814	O–Mo_2	Stretching	[9]
	983	O=Mo	Stretching	[9]
MoS_2	144	Lattice mode	–	[35]
	275	O=Mo	Bending	[35]
	370	MoS_2	in-plane E_{2g}	[39]
	400	MoS_2	out-of-plane A_{1g}	[39]
	653	O–Mo_3	Stretching	[35]
	814	O–Mo_2	Stretching	[35]
	983	O=Mo	Stretching	[35]
MoS_2@Ti_3C_2	144	Lattice mode	–	[9]
	275	O=Mo	Bending	[9]
	370	MoS_2	in-plane E_{2g}	[39]
	400	MoS_2	out-of-plane A_{1g}	[39]
	653	O-Mo_3	Stretching	[9]
	814	O-Mo_2	Stretching	[9]
	983	O=Mo	Stretching	[9]
MoS_2@Mo_2TiC_2	144	Lattice mode	–	[9]
	275	O=Mo	Bending	[9]
	370	MoS_2	in-plane E_{2g}	[39]
	400	MoS_2	out-of-plane A_{1g}	[39]
	653	O–Mo_3	Stretching	[9]
	814	O–Mo_2	Stretching	[9]
	983	O=Mo	Stretching	[9]

© 2024 The Authors. ChemElectroChem published by Wiley-VCH GmbH

21960216, 2024, 6, Downloaded from https://chemistry-europe.onlinelibrary.wiley.com/doi/10.1002/celc.202300673 by University Of Padova Center Di, Wiley Online Library on [04/02/2025]. See the Terms and Conditions (https://onlinelibrary.wiley.com/terms-and-conditions) on Wiley Online Library for rules of use; OA articles are governed by the applicable Creative Commons License

regions are observed, confirming that MoS_2 covers the MXene supports. Similar results have been already reported in the literature.[21,27] Figures 4 a, c and e depict the deconvolution of the Mo 3d region for MoS_2@Mo_2TiC_2, MoS_2@Ti_3C_2 and MoS_2, respectively, whereas Figures 4 b, d and f show the analysis of the corresponding S 2p spectra. For the three samples, the Mo 3d region can be separated into two components. The first one located at 228.6 eV and 231.8 eV, assigned to the Mo $3d_{5/2}$ and Mo $3d_{3/2}$ of Mo^{4+} in MoS_2; and the second at 232.1 and 235.4 eV, associated to the presence of a small amount (< 5 at.%) of MoO_3 on the surface of MoS_2 due to the air exposure.[21,27,43] Regarding the S 2p spectra, two signals are observed at 161.4 eV (S $2p_{3/2}$) and 162.7 eV (S $2p_{1/2}$), which are assigned to S^{2-} of MoS_2. No oxygen species associated to the presence of sulphur oxides were detected. The relative abundance of these species is reported in Table 4.

Electrochemical characterisation

Cyclic voltammograms of the synthesised catalysts in O_2-free (**black line**) and O_2-saturated (**blue line**) supporting electrolyte can be seen in Figure 5. Deposition of MoS_2 on MXenes induced an enhancement in the capacitive currents, which is attributed to the increase in the surface area generated by the MoS_2 nanoparticle structure. SEM images (Figure 1) demonstrated a high roughness of MoS_2 structures, thus explaining the increase in the active surface area for these materials. In the case of cyclic voltammograms registered in O_2-saturated electrolyte, a cathodic peak was detected for all studied materials, as reported in Figure 5, assigned to the reduction of the oxygen present in the supporting electrolyte.[7] MoS_2@Ti_3C_2 exhibited the most positive peak potential values (0.62 V), suggesting that the high activity for this material is originated from the synergy between both components (as the peak potential for both MoS_2 and Ti_3C_2 is located around 0.57 V). Remarkably, pure MoS_2 revealed a positive shift of 16 mV in the cathodic peak during the second and subsequent scans, indicating an activation for this catalyst during the cycling process in presence of oxygen.

ORR activity on the MXenes, MoS_2@MXene, MoS_2 and commercial Pt/C materials was evaluated with the rotating ring-disk electrode (RRDE) in alkaline media (Figure 6). As expected, Pt/C developed the highest reduction current densities at the disk, j_{Disk} (Figure 6a). For the other materials, a plateau was observed in the disk current densities between 0.4 and 0.6 V *vs* RHE. Usually, this is related with an inhibition process caused by the adsorption of HOO^- on the catalyst surface (see below, reaction (2)).[44] The currents registered at the ring confirm this hypothesis, since an increase of the current is observed in this potential range that decreases at lower potentials due to the further reduction of HOO^- to OH^-. The most positive onset potentials (E_{onset}) for the ORR were developed by MoS_2@Ti_3C_2 and MoS_2@Mo_2TiC_2 (see Table 5), but still far from that of Pt/C. On the other hand, it is remarkable that current densities recorded at the disk for the composite materials are higher than those for the pure materials, verifying the synergetic effect between MoS_2 and the MXenes. Concerning the activity of composite materials, Yang and co-workers synthesised multi-walled carbon nanotubes decorated with MoS_2 and $Ti_3C_2T_x$ quantum dots and studied the ORR on these catalysts in alkaline media.[28] These authors found current densities values (j_L) between 2 and 4 mA cm^{-2} at 0.4 V *vs* RHE in 1.0 M KOH. Maximum current densities observed in this work were around 2.6 mA cm^{-2}, suggesting that our composites provide a similar catalytic activity to that reported in this reference.[28]

MoS_2 and MXenes as pure materials did not overcome the j_{Disk} developed by the composites, as appreciated from their

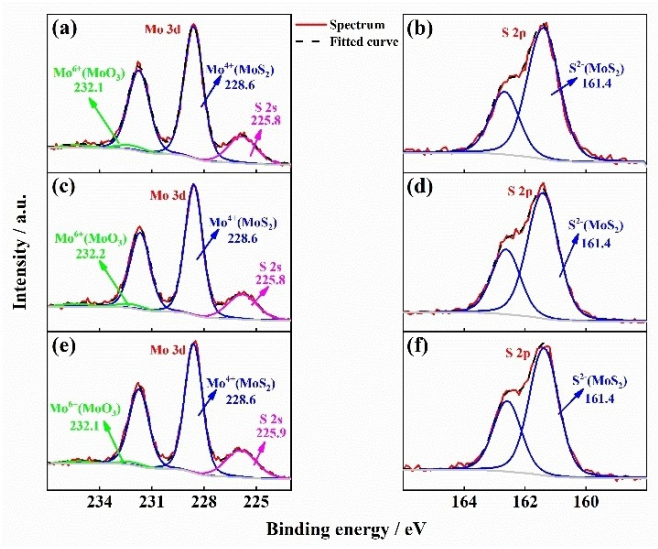

Figure 4. (a,c,d) Mo 3d and (b,d,f) S 2p XPS regions, and their corresponding separation into single chemical components. (a,b) MoS_2@Mo_2TiC_2; (c,d) MoS_2@Ti_3C_2; (e,f) MoS_2.

Table 4. Analysis of the Mo 3d and S 2p XPS regions. For each component, the binding energy and the at. % are reported.

Material	MoS_2@Mo_2TiC_2			MoS_2@Ti_3C_2			MoS_2		
Element	Binding energy (eV)	Assignment	Relative abundance (%)	Binding energy (eV)	Assignment	Relative abundance (%)	Binding energy (eV)	Assignment	Relative abundance (%)
Mo (3d)	228.6	$Mo^{4+}(MoS_2)$	95.1	228.6	$Mo^{4+}(MoS_2)$	95.4	228.6	$Mo^{4+}(MoS_2)$	96.7
	232.1	$Mo^{6+}(MoO_3)$	4.9	232.2	$Mo^{6+}(MoO_3)$	4.6	232.1	$Mo^{6+}(MoO_3)$	3.3
S (2p)	161.4	$S^{2-}(MoS_2)$	100	161.4	$S^{2-}(MoS_2)$	100	161.4	$S^{2-}(MoS_2)$	100
S (2 s)	225.8	S 2s	***	225.8	S 2s	***	225.9	S 2 s	***

© 2024 The Authors. ChemElectroChem published by Wiley-VCH GmbH

21960216, 2024, 6, Downloaded from https://chemistry-europe.onlinelibrary.wiley.com/doi/10.1002/celc.202300673 by University Of Padova Center Di, Wiley Online Library on [04/02/2025]. See the Terms and Conditions (https://onlinelibrary.wiley.com/terms-and-conditions) on Wiley Online Library for rules of use; OA articles are governed by the applicable Creative Commons License

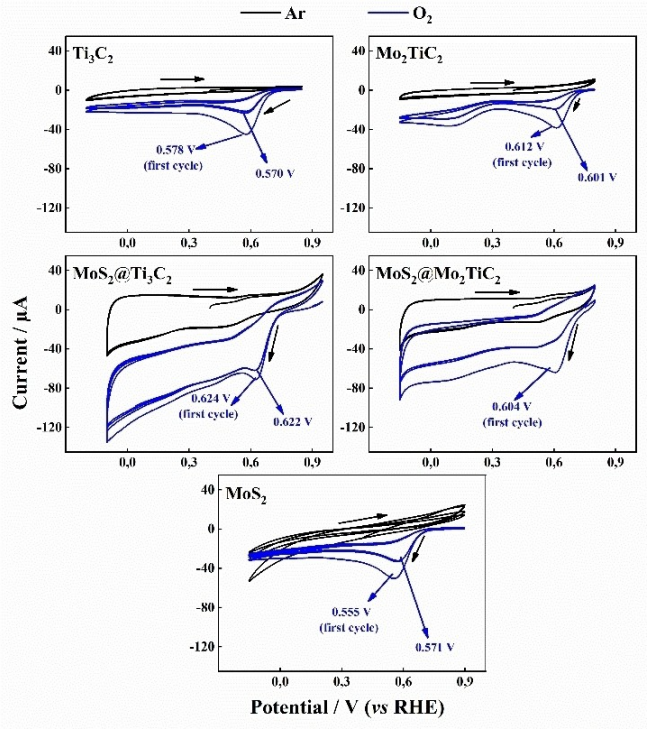

Figure 5. Cyclic voltammograms of MXenes, MoS_2 and MoS_2@MXenes in 0.1 M NaOH saturated with argon (black) and oxygen (blue). Scan rate: 0.01 $V s^{-1}$.

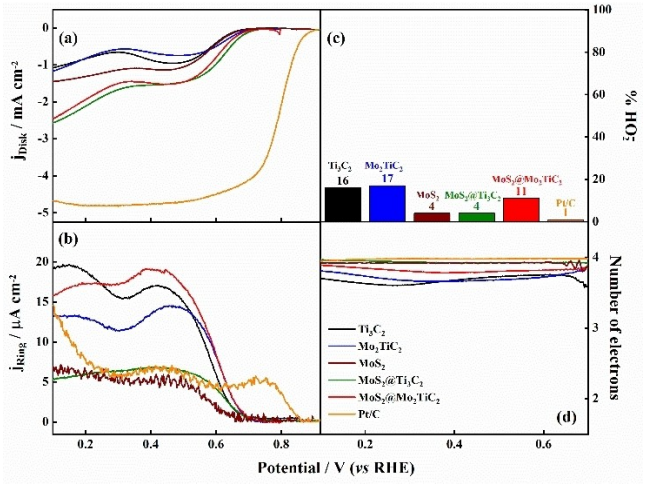

Figure 6. RRDE polarisation curves for O_2 reduction at 0.002 $V s^{-1}$ and 1600 rpm in 0.1 M NaOH at 25 °C for the studied materials. (a) Current densities at the disk; (b) current densities for hydroperoxide anion oxidation at the Pt ring (E_{ring} = at 1.20 *vs* RHE); (c) hydroperoxide anion percentage produced at 0.4 V *vs* RHE; and (d) number of electrons involved in the ORR.

polarisation curves in Figure 6a. In fact, MXenes developed the lowest activity toward the ORR, as can be observed from the parameters collected in Table 5. j_{Disk} observed for MXenes in this paper were similar to those reported by Lin et al.[7] and Li and co-workers,[18] who evaluated the ORR performance on Ti_3C_2 and Mo_2TiC_2, respectively, finding j_L values around 1.5 $mA cm^{-2}$.

Another proof of the synergy between MXenes and MoS_2 and the resulting increase in the catalytic activity towards ORR are the potential values measured at 1 $mA cm^{-2}$. MoS_2@MXenes materials exhibited more positive values than those observed for MXenes and similar to those for MoS_2, indicating that the performance depends essentially on this specie located at the surface of the catalyst. Exchange current density was also calculated to determine how fast the ORR occurs in the different materials, finding that $MoS_2@Mo_2TiC_2$ developed the highest value among the synthesised catalysts.

Regarding the current densities detected at the Pt ring during the RRDE experiments (Figure 6b), which are related to the oxidation of HOO^- formed on the disk,[45] all MXene-based materials developed HOO^- percentages below 20%. Thus, in Figure 6c can be seen the values at 0.4 V *vs* RHE, with the best response observed for $MoS_2@Ti_3C_2$ (4%), like MoS_2 (4%), which were lower than $MoS_2@Mo_2TiC_2$ (11%). The number of electrons involved in the ORR (Figure 6d) for the composites is near 4 (especially for $MoS_2@Ti_3C_2$) in the whole potential range considered, i.e. the formation of water prevails for these materials, whereas "pure" MXenes address values around 3.7, which indicates a lower selectivity for water production.

Potential *vs* logarithm of current density plots was used to obtain Tafel slopes at low and high overpotentials (η) and the results are represented in Figures 7a and 7b, respectively. Previous theoretical studies have shown that, from the value of

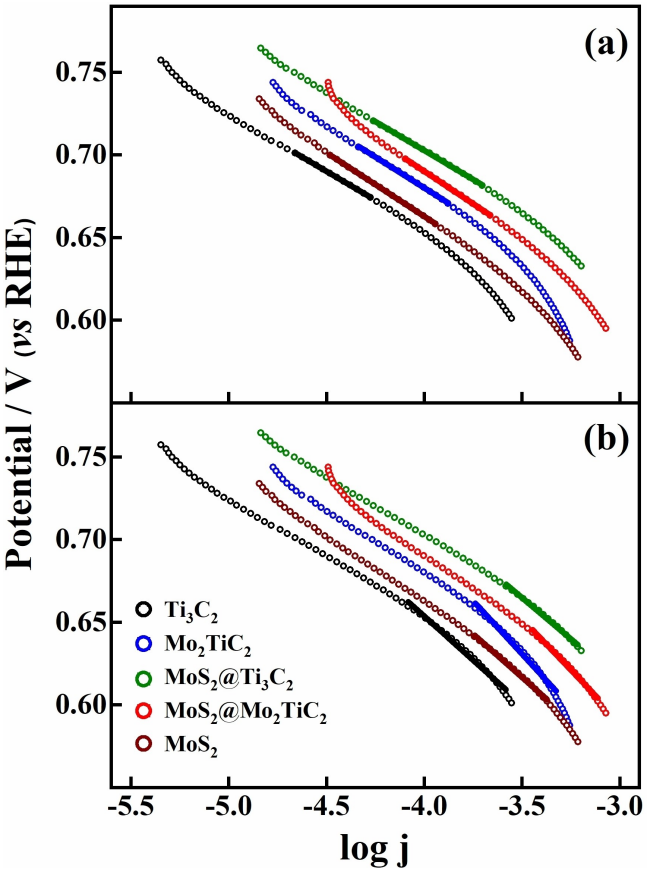

Figure 7. Tafel plots for ORR in 0.1 M NaOH for the different studied materials at (a) low and (b) high overpotentials from Figure 6a.

© 2024 The Authors. ChemElectroChem published by Wiley-VCH GmbH

21960216, 2024, 6, Downloaded from https://chemistry-europe.onlinelibrary.wiley.com/doi/10.1002/celc.202300673 by University Of Padova Center Di, Wiley Online Library on [04/02/2025]. See the Terms and Conditions (https://onlinelibrary.wiley.com/terms-and-conditions) on Wiley Online Library for rules of use; OA articles are governed by the applicable Creative Commons License

21960216, 2024, 6, Downloaded from https://chemistry-europe.onlinelibrary.wiley.com/doi/10.1002/celc.202300673 by University Of Padova Center Di, Wiley Online Library on [04/02/2025]. See the Terms and Conditions (https://onlinelibrary.wiley.com/terms-and-conditions) on Wiley Online Library for rules of use; OA articles are governed by the applicable Creative Commons License

Table 5. Electrochemical parameters obtained from LSV in Figure 6a.

Catalyst	E_{onset}/V_{RHE}	E at −1 mA cm^{-2}/V_{RHE}	$j_{at\ 0\ V\ vs\ RHE}$/mA cm^{-2}	j_0/mA cm^{-2}
Ti_3C_2	0.70	0.13	−1.1	2.7×10^{-10}
Mo_2TiC_2	0.71	0.15	−1.2	3.2×10^{-9}
MoS_2@Ti_3C_2	0.73	0.58	−2.6	2.8×10^{-9}
MoS_2@Mo_2TiC_2	0.72	0.60	−2.5	1.1×10^{-8}
MoS_2	0.70	0.52	−1.5	7.7×10^{-9}
Pt/C	0.93	0.83	−4.7	1.9×10^{-7}

these slopes, it is possible to elucidate the rate determining step (*rds*) for the ORR.[46–49] Tafel slope values for the catalysts studied in this work are reported in Table 6. The change in the Tafel slopes with the applied potential indicates that the mechanism depends on this parameter. This ORR mechanism proposed in alkaline media involves a dissociative pathway:[50]

$$O_2 \rightarrow O_{2(ads)} \quad (1)$$

$$O_{2(ads)} + H_2O + e^- \rightarrow OOH_{(ads)} + OH^- \quad (2)$$

$$OOH_{(ads)} \rightarrow O_{(ads)} + OH_{(ads)} \quad (3)$$

$$OOH_{(ads)} + e^- \rightarrow OOH^- \quad (4)$$

$$O_{2(ads)} + H_2O + e^- \rightarrow OH_{(ads)} + OH^- \quad (5)$$

$$OH_{(ads)} + e^- \rightarrow OH^- \quad (6)$$

Tafel slope values at low η near to 60 mV dec^{-1} indicate that *rds* corresponds to a chemical step after an electrochemical one.[46–49] In the proposed mechanism previously described, this step corresponds to equation 3. On the other hand, values near to 120 mV dec^{-1} can be explained considering equation 2 as the *rds*, where hydroperoxide anion is adsorbed on the catalyst surface.[46–49] For the materials studied in the present work, values determined for the Tafel slopes at low overpotentials are in the range of 67–78 mV dec^{-1} (Table 6). In the case of Ti_3C_2 and MoS_2@Ti_3C_2, Tafel slopes resulted in 67 and 69 mV dec^{-1}, respectively, indicating that the ORR in these materials follows a mechanism where the *rds* is the dissociation of $OOH_{(ads)}$ (equation 3). On the other hand, for Mo_2TiC_2, MoS_2@Mo_2TiC_2 and MoS_2, Tafel slopes approach 80 mV dec^{-1}, value that can be explained assuming the competence between the dissociation of $OOH_{(ads)}$ (equation 3), with an expected Tafel slope of 60 mV dec^{-1},[50] and the blocking of the catalysts surface active sites by $OOH_{(ads)}$ (equation 2),[51,52] with a Tafel slope value of 120 mV dec^{-1}. This result accounts for the relevance of hydroperoxide anion presence as intermediate during the ORR for the studied catalysts.

Table 6. Tafel slope values determined for the studied materials.

Catalyst	Tafel slope/mV dec^{-1} (low η)	Tafel slope/mV dec^{-1} (high η)
Ti_3C_2	67	106
Mo_2TiC_2	74	129
MoS_2@Ti_3C_2	69	100
MoS_2@Mo_2TiC_2	78	124
MoS_2	77	105

The increase in the overpotential leads in the obtaining of higher Tafel slope values, overcoming 100 mV dec^{-1}. Since these values are close to 120 mV dec^{-1}, it can be concluded that *rds* at high overpotentials for all the studied materials corresponds to equation 2.[51,52]

Long-term stability tests were addressed to evaluate the performance of the catalysts, by applying 5000 potential cycles between 0 and 0.85 V *vs* RHE at 100 mV s^{-1} in the O_2-saturated supporting electrolyte. The current densities registered at the disk, j_{Disk}, are shown in Figure 8a. j_{Disk} decreased for MoS_2@Mo_2TiC_2 and MoS_2@Ti_3C_2 composites in the whole potential range. Furthermore, shifts in their E_{onset} and potential at −1 mA cm^{-2} towards more negative values were observed. These results indicate a detriment in the activity towards the ORR after the cycling treatment. A similar trend was observed for MoS_2 between 0.8 and 0.2 V *vs* RHE, however, at potentials

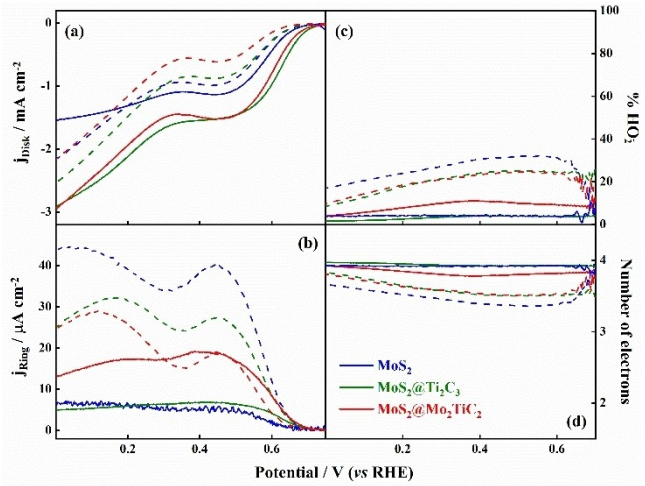

Figure 8. RRDE polarisation curves for O_2 reduction at 0.002 V s^{-1} and 1600 rpm in 0.1 M NaOH at 25 °C for the studied materials, before (solid lines) and after (dashed lines) long-term stability tests. (a) Current densities at the disk; (b) current densities for hydroperoxide anion oxidation at the Pt ring (E_{ring} = at 1.20 *vs* RHE); (c) hydroperoxide anion percentage; and (d) number of electrons involved in the ORR.

© 2024 The Authors. ChemElectroChem published by Wiley-VCH GmbH

more negative than 0.2 V, an increase in the current densities for the as-treated MoS_2 catalyst was registered.

The change in the activity of these materials altered the currents registered at the Pt ring, j_{Ring}, as can be seen in Figure 8b. In all cases, the cycling process induced an enhancement in the current densities associated with the production of HOO^-, indicating that the materials undergone a chemical/structural change after the tests, favouring the 2-electron path. The HOO^- production percentage (Figure 8c) for $MoS_2@Mo_2TiC_2$ and $MoS_2@Ti_3C_2$ is increased up to around 24% in the 0.6–0.4 V potential range, decreasing at more negative potentials, whereas MoS_2 shows a similar trend but achieving 32% of HOO^-.

The number of electrons depicted in Figure 8d verifies the increase in the formation of HOO^- for all studied catalysts after potential cycling, since lower number of electrons was observed in the whole potential range. At 0.4 V, this parameter changed from 3.9 to 3.4 and 3.5 for MoS_2 and $MoS_2@Ti_3C_2$, respectively, whereas the number of electrons for $MoS_2@Mo_2TiC_2$ changed from 3.8 to 3.5.

SEM-EDX mapping analysis was performed after the long-term stability tests for the MoS_2@MXene materials to get information about the detriment in the activity of the materials after the cycling process. Table SI1 shows a slight decrease in the atomic content of Mo and S after the cycling treatment, although their atomic ratio was kept as Mo:S = 1:2. In fact, no significant changes were observed in the EDX mapping signals of the materials, as can be appreciated in Figure 9. On the other hand, the SEM images showed the formation of few agglomerates after the cycling treatment (Figures 9b and 9d).

To further explain the changes provoked by the long-term stability tests, electrochemical surface areas (ECSA) were calculated before and after the cycling treatment. A detailed description of the calculations performed to determine these ECSA values is reported in the Supporting Information. Table SI2 reports the ECSA values, indicating in all cases, changes below 14% in the calculated estimated ECSA after the test, corroborating that no drastic morphological changes occurred in the catalysts. Bearing in mind that no significant changes were observed in both the composition and morphological features of the catalysts, before and after the cycling treatment, further studies will be performed in the future to determine the reason for the changes in the activity of the materials, which provoke the increase in HOO^- production.

Conclusions

Two composites of MoS_2 coating Mo_2TiC_2 and Ti_3C_2 were synthesised to assess its performance as catalysts for the ORR.

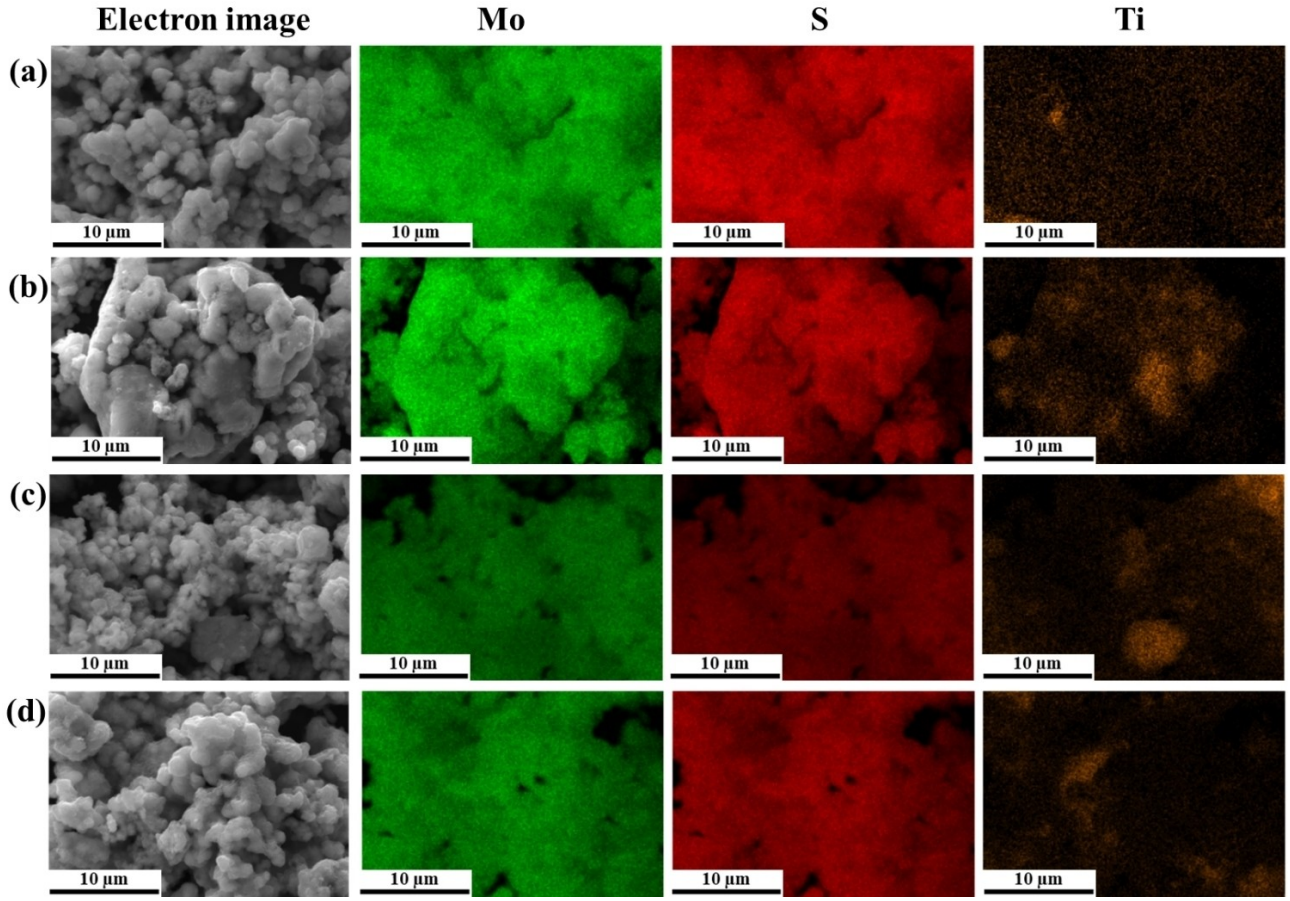

Figure 9. SEM and EDX mapping images for $MoS_2@Mo_2TiC_2$ before (a) and after the long-term stability test (b). (c) images for $MoS_2@Ti_3C_2$ before and (d) after the long-term stability test.

© 2024 The Authors. ChemElectroChem published by Wiley-VCH GmbH

21960216, 2024, 6, Downloaded from https://chemistry-europe.onlinelibrary.wiley.com/doi/10.1002/celc.202300673 by University Of Padova Center Di, Wiley Online Library on [04/02/2025]. See the Terms and Conditions (https://onlinelibrary.wiley.com/terms-and-conditions) on Wiley Online Library for rules of use; OA articles are governed by the applicable Creative Commons License

The synthesis route led to MoS_2 nanospheres supported on MXenes, which was evidenced by means of SEM-EDX mapping, the disappearing of the vibration modes of MXenes measured by Raman spectroscopy and the predominance of XPS transitions attributed to MoS_2. RRDE experiments demonstrated a significant enhancement of ORR activity in these composites compared to the MXenes and MoS_2 individual catalysts, as could be demonstrated from the current densities collected on the disk. The presence of MoS_2 resulted in a decrease in the production of HOO^- and an increase in the number of electrons involved in ORR in the composites with respect to the MXene, achieving values near to 4 associated to the production of water as main product.

Tafel slopes at low overpotentials indicate that the rate determining step could be either the dissociation of $OOH_{(ads)}$ or the blocking of the active sites by HOO^-. On the other hand, application of high overpotentials leads to the formation of adsorbed HOO^- by reduction of oxygen adsorbed on the catalysts as *rds* for all the studied materials.

Long-term stability tests showed that the yield of HOO^- increases after the potential cycling treatment producing a decrease in the current densities recorded. SEM-EDX analysis and ECSA values of the MoS_2@MXene materials before and after testing allow to conclude that changes in the morphology and compositions observed cannot justify the drop in the activity. Considering the improvement in the activity of composites respect to individual materials, and its low cost due to the absence of noble metals, it can be stated that these hybrid materials could be the starting point for the design of noble metal-free catalysts based on MXenes composites with tuneable activity toward ORR.

Experimental Section

MXenes were synthesized by 50 wt% HF (≥48%, Sigma-Aldrich) chemical etching of MAX phases (Mo_2TiAlC_2 and Ti_3AlC_2, 98% and 99%, respectively, Laizhou Kai Kai Ceramic Materials Co.), during 48 hours at different temperatures (55 °C and 45 °C for Mo_2TiC_2 and Ti_3C_2, respectively). Once the etching was completed, the mixture was dispersed by ultrasound in ultrapure water (18.2 MΩ cm^{-2}, Millipore®) for 90 minutes. Afterwards, the products were washed several times with ultrapure water to reach pH 6. Finally, the obtained powder was dried in an oven at 80 °C overnight.

MoS_2@MXenes composites were prepared following a hydrothermal method. First, 0.167 mmol of MXenes were dispersed in 20 mL ultrapure water for 30 min. Then 0.292 mmol of $(NH_4)_6Mo_7O_{24}\cdot 4H_2O$ (>99%, Sigma-Aldrich) and 7.34 mmol of thiourea (>99%, Sigma-Aldrich) were added under stirring. This mixture was transferred into a steel autoclave and heated at 210 °C for 18 h. The obtained precipitate was separated by centrifugation and washed with ethanol/milli-Q water and dried overnight at 60 °C.

X-ray diffraction analyses were performed using a PANalytical X'PERT-Pro diffractometer for powder samples, applying Cu-K_α radiation (λ = 0.1550 nm) at 40 kV and 20 mA. The scans were collected at 2.4° min^{-1} for 2θ values between 5° and 90°. Crystallite size and interplanar size of the catalysts were determined using Scherrer equation (eq. 7) and Bragg's law (eq. 8), respectively:[1]

$$L_c = \frac{0.9\lambda}{\beta_{1/2}\cos\cos\theta} \quad (7)$$

$$2d_{hkl}sen\ \theta = n\lambda \quad (8)$$

where d_{hkl} is the interplanar distance, λ is the wavelength of the incident wave, q is the scattering angle and $\beta_{1/2}$ is the full width at half maximum.

In order to confirm the presence of metal oxides in the catalysts, Raman experiments were performed, employing a SPELEC RAMAN (Metrohm DropSens) instrument with a green laser (λ = 532 nm) and a Raman probe. The equipment was controlled by means of the software DropView Spelec applying 10 scans to obtain the spectra for each material.

Scanning electron microscopy (SEM) coupled with energy-dispersive X-ray (EDX) analysis was used to determine the morphology and compositions of the synthesised materials. A scanning electron microscope Zeiss Evo 15 coupled to an Oxford X–MAX analyser with a 50 mm^2 Si detector was employed. Different probe convergence semi-angles were used to perform the EDX mapping, which were taken each 35°. Probe voltage was set to 20 kV and the aperture was fixed to 120 μm. Each image was obtained with a size of 256×192 pixels.

XPS measurements were performed in a custom designed UHV system equipped with an EA 125 Omicron electron analyser with five channeltrons, working at a base pressure of 10^{-10} mbar. Core level photoemission spectra (S 2p, Mo 2d, C 1s, Ti 2p, O 1s regions) were collected in normal emission at room temperature with a non-monochromatised Al Kα X-ray source (1486.7 eV) and using 0.1 eV steps, 0.5 s collection time and 20 eV pass energy. The quantitative analysis of the XPS measurements was performed with CasaXPS software, after fitting the experimental data with Gaussian-Lorentzian curves.

Electrochemical measurements were performed using an Autolab® PGSTAT302 N potentiostat-galvanostat. A three-electrode electrochemical cell containing a glassy carbon bar as a counter electrode and a reversible hydrogen electrode (RHE) placed inside a Luggin capillary as a reference electrode was used. As working electrode, a glassy carbon disk (disk diameter 5 mm)/Pt ring RRDE electrode coupled to a rotating disk-ring setup (RRDE, PINE Research Instrumentation) was employed. The collection efficiency of the Pt ring was determined as N = 0.22. On the glassy carbon disk, 20 μL-aliquot of an ink composed by 2 mg of the catalyst with 15 μL of Nafion® (5 wt.%, Sigma-Aldrich) and 500 μL of ultra-pure water was deposited and dried at room temperature with a nitrogen flow. All the experiments were carried out in 0.1 M NaOH (99,997%, Sigma-Aldrich).

Before the evaluation of the activity toward ORR on the catalysts, the electrolyte was deoxygenated by bubbling Ar (99.999%, Alpha GAZ, Air Liquide) for 25 minutes and afterwards, a cyclic voltammogram at 0.01 V s^{-1} was collected. Due to the different stability window of each material, a different potential range was utilised for the cyclic voltammetry experiments as follows: −0.15 to 0.8 V for Mo_2TiC_2, −0.2 to 0.85 V for Ti_3C_2, −0.15 to 0.8 V for MoS_2@Mo_2TiC_2, −0.1 a 0.95 V for MoS_2@Ti_3C_2 and −0.15 a 0.9 V for MoS_2. Afterwards, O_2 (99.995%, Air Liquide) was bubbled into the supporting electrolyte for 45 min at 1.0 V. This procedure was repeated before each experiment and during the measurements performed by cyclic voltammetry. Then, steady-state polarisation curves were registered at 2 mV s^{-1} between 1.0 and 0 V using 1600 rpm as rotating speed. Polarisation curves were also recorded in absence of O_2. Currents at the Pt ring corresponding to the oxidation at 1.20 V_{RHE} of the hydroperoxide anion formed on the

© 2024 The Authors. ChemElectroChem published by Wiley-VCH GmbH

21960216, 2024, 6, Downloaded from https://chemistry-europe.onlinelibrary.wiley.com/doi/10.1002/celc.202300673 by University Of Padova Center Di, Wiley Online Library on [04/02/2025]. See the Terms and Conditions (https://onlinelibrary.wiley.com/terms-and-conditions) on Wiley Online Library for rules of use; OA articles are governed by the applicable Creative Commons License

catalysts at the disk, were simultaneously measured to calculate the conversion of oxygen to this intermediate, according to eq. 9:

$$\% HO_2^- = 200\frac{j_{Ring}/N}{j_{Disk} + j_{Ring}/N} \quad (9)$$

where j_d is the current density generated at the disk, j_r is the ring current density produced at the ring, and N is the current collection efficiency of the Pt ring. These currents were also employed to calculate the number of electrons by means of eq. 10:

$$n = 4\frac{j_{Disk}}{j_{Disk} + j_{Ring}/N} \quad (10)$$

Long-term stability tests were addressed to evaluate the stability of the studied materials. 5000 cycles were recorded between 0 and 0.85 V *vs* RHE, at 100 mV s^{-1} in the O_2-saturated supporting electrolyte, while an O_2 atmosphere was kept. O_2 was bubbled during 45 min before and after the cycling procedure, and polarisation curves at 1600 rpm were recorded. All the currents related to these experiments were normalised by the working electrode geometric area.

Acknowledgements

This work has been supported by the Ministerio de Ciencia e Innovación (MCIN) under projects PCI2020-112249 and PID2020-117586RB–I00 funded by MCIN/AEI/10.13039/501100011033. The author thanks SEGAI for its collaboration with the physical characterisation of the studied materials. S.D. and Y.R.D. thank to ACIISI (Agencia Canaria de Investigación, Innovación y Sociedad de la Información) and the European Social Fund (ESF) (Operative Integrated Program of Canary Islands 2021–2027, Area 3 Priority Theme 74 (85%)) for the predoctoral contracts (TESIS2022010136 and TESIS2022010103). JCC is indebted to ULL for the "María Zambrano" Research Contract UNI/551/2021 and Project for Young Researchers no. 2022/20204.

Conflict of Interests

The authors declare no conflict of interest.

Data Availability Statement

The data that support the findings of this study are available on request from the corresponding author. The data are not publicly available due to privacy or ethical restrictions.

Keywords: 2D MXenes · MoS_2 composites · ORR · fuel cells

[1] J. C. Calderón, L. Ndzuzo, B. J. Bladergroen, S. Pasupathi, *Mater. Today: Proc.* **2018**, *5*, 10551.
[2] V. Viswanathan, H. A. Hansen, J. Rossmeisl, J. K. Nørskov, *ACS Catal.* **2012**, *2*, 1654.
[3] T. P. Johansson, E. T. Ulrikkeholm, P. Hernández-Fernández, P. Malacrida, H. A. Hansen, A. S. Bandarenka, et al., *Top. Catal.* **2013**, *57*, 245.
[4] X. Ge, A. Sumboja, D. Wuu, T. An, B. Li, F. W.T Goh, T. S. Andy Hor, Y. Zong, Z. Liu, *ACS Catal.* **2015**, *5*, 4643.
[5] Z. Chen, D. Higgins, A. Yu, L. Zhang, J. Zhang, *Energy Environ. Sci.* **2011**, *4*, 3167.
[6] F. Jaouen, E. Proietti, M. Lefèvre, R. Chenitz, J. P. Dodelet, G. Wu, H. T. Chung, C. M. Johnston, P. Zelenay, *Energy Environ. Sci.* **2011**, *4*, 114.
[7] H. Lin, L. Chen, X. Lu, H. Yao, Y. Chen, J. Shi, *Sci. China Mater.* **2019**, *62*, 662.
[8] H. W. Wang, M. Naguib, K. Page, D. J. Wesolowski, Y. Gogotsi, *Chem. Mater.* **2016**, *28*, 349.
[9] S. Delgado, Y. Remedios-Díaz, J. C. Calderón, S. Díaz-Coello, M. C. Arévalo, G. García, E. Pastor, *Int. J. Hydrogen Energy*, accepted, DOI: 10.1016/j.ijhydene.2023.11.288.
[10] B. Anasori, M. R. Lukatskaya, Y. Gogotsi, *Nat. Rev. Mater.* **2017**, *2*, 16098.
[11] O. Mashtalir, M. Naguib, V. N. Mochalin, Y. Dall'Agnese, M. Heon, M. W. Barsoum, Y. Gogotsi, *Nat. Commun.* **2013**, *4*, 1.
[12] W. T. Wang, N. Batool, T. H. Zhang, J. Liu, X. F. Han, J. H. Tian, R. Yang, *J. Mater. Chem. A.* **2021**, *9*, 3952.
[13] Y. Wen, C. Ma, Z. Wei, X. Zhu, Z. Li, *RSC Adv.* **2019**, *9*, 13424.
[14] X. Huang, M. Song, J. Zhang, J. Zhang, W. Liu, C. Zhang, W. Zhang, D. Wang, *Nano Res.* **2022**, *15*, 3927.
[15] X. Xie, S. Chen, W. Ding, Y. Nie, Z. Wei, *Chem. Commun.* **2013**, *49*, 10112.
[16] C. Zhang, B. Ma, Y. Zhou, C. Wang, *J. Electroanal. Chem.* **2020**, *865*, 114142.
[17] H. Xu, D. Wang, P. Yang, A. Liu, R. Li, Y. Li, L. Xiao, X. Ren, J. Zhang, M. An, *J. Mater. Chem. A.* **2020**, *8*, 23187.
[18] Z. Li, Z. Zhuang, F. Lv, H. Zhu, L. Zhou, M. Luo, J. Zhu, Z. Lang, S. Feng, W. Chen, L. Mai, S. Guo, *Adv. Mater.* **2018**, *30*, 1803220.
[19] R. Cao, R. Thapa, H. Kim, X. Xu, K. M. Gyu, Q. Li, N. Park, M. Liu, J. Cho, *Nat. Commun.* **2014**, *4*, 2076.
[20] Y. Zhang, H. Jiang, Y. Lin, H. Liu, Q. He, C. Wu, T. Duan, L. Song, *Adv. Mater. Interfaces* **2018**, *5*, 1800392.
[21] S. Wei, Y. Fu, M. Liu, H. Yue, S. Park, Y. H. Lee, H. Li, F. Yao, *NPJ 2D Mater. Appl.* **2022**, *6*, 25.
[22] X. Wang, W. You, L. Yang, G. Chen, Z. Wu, C. Zhang, Q. Chen, R. Che, *Nanoscale Adv.* **2022**, *4*, 3398.
[23] G. Ghanashyam, H. K. Jeong, *Inorg. Chim. Acta* **2022**, *541*, 121098.
[24] Q. Ma, H. Qiao, Z. Huang, F. Liu, C. Duan, Y. Zhou, G. Liao, X. Qi, *Appl. Surf. Sci.* **2021**, *562*, 150213.
[25] M. A. Kosnan, M. A. Azam, N. E. Safie, R. F. Munawar, A. Takasaki, *Micromachines* **2022**, *13*, 1837.
[26] S. Xie, X. Fei, J. Wang, Y. C. Zhu, J. Liu, X. Du, X. Liu, L. Dong, Y. Zhu, J. Pan, B. Dong, J. Sha, Y. Luo, W. Sun, W. Xue, *Adv. Sci.* **2023**, *10*, 2206494.
[27] T. Guo, Y. Lei, X. Hu, G. Yang, J. Liang, Q. Huang, X. Li, M. Liu, X. Zhang, Y. Wei, *Appl. Surf. Sci.* **2022**, *588*, 152597.
[28] X. Yang, Q. Jia, F. Duan, B. Hu, M. Wang, L. He, Y. Song, Z. Zhang, *Appl. Surf. Sci.* **2019**; *464*, 78.
[29] A. Arunchander, S. Gouse Peera, A. K. Sahu, *J. Power Sources* **2017**, *353*, 104.
[30] C. Tang, L. Zhong, B. Zhang, H. F. Wang, Q. Zhang, *Adv. Mater.* **2018**, *30*, 1705110.
[31] M. Naguib, V. N. Mochalin, M. W. Barsoum, Y. Gogotsi, *Adv. Mater.* **2014**, *26*, 992.
[32] M. Naguib, O. Mashtalir, J. Carle, V. Presser, J. Lu, L. Hultman, Y. Gogotsi, M. W. Barsoum, *ACS Nano.* **2012**, *6*, 1322.
[33] M. H. Tran, T. Schäfer, A. Shahraei, M. Dürrschnabel, L. Molina-Luna, U. I. Kramm, C. S. Birkel, *ACS Appl. Energ. Mater.* **2018**, *1*, 3908.
[34] M. Naguib, M. Kurtoglu, V. Presser, J. Lu, J. Niu, M. Heon, L. Hultman, Y. Gogotsi, M. W. Barsoum, *Adv. Mater.* **2011**, *23*, 4248.
[35] M. Benchakar, V. Natu, T. A. Elmelegy, M. Sokol, J. Snyder, C. Comminges, C. Morais, S. Célérier, A. Habrioux, M. W. Barsoum, *J. Electrochem. Soc.* **2020**, *167*, 12450.
[36] J. Bai, B. Zhao, S. Lin, K. Li, J. Zhou, J. Dai, X. Zhu, Y. Sun, *Nanoscale* **2020**, *12*, 1144.
[37] N. Jahan, S. Hussain, H. U. Rahman, I. Manzoor, S. Pandey, K. Habib, S. K. Ali, R. Pandita, C. Upadhyay, *J. Multidiscip. Appl. Nat. Sci.* **2021**, *1*, 13.
[38] J. Chen, Y. Xia, J. Yang, B. Chen, *Appl. Phys. A Mater. Sci. Process.* **2018**, *124*, 1.
[39] C. Chen, X. Xie, B. Anasori, A. Sarycheva, T. Makaryan, M. Zhao, P. Urbankowski, L. Miao, J. Jiang, Y. Gogotsi, *Angew. Chem. Int. Ed.* **2018**, *57*, 1846.
[40] L. Seguin, M. Figlarz, R. Cavagnat, J. C. Lassègues, *Spectrochim. Acta Part A* **1995**, *51*, 1323.

© 2024 The Authors. ChemElectroChem published by Wiley-VCH GmbH

21960216, 2024, 6, Downloaded from https://chemistry-europe.onlinelibrary.wiley.com/doi/10.1002/celc.202300673 by University Of Padova Center Di, Wiley Online Library on [04/02/2025]. See the Terms and Conditions (https://onlinelibrary.wiley.com/terms-and-conditions) on Wiley Online Library for rules of use; OA articles are governed by the applicable Creative Commons License

[41] X. Zhang, X. F. Qiao, W. Shi, J. B. Wu, D. S. Jiang, P. H. Tan, *Chem. Soc. Rev.* **2015**, *44*, 2757.
[42] S. H. Lee, H. M. Cheong, M. J. Seong, P. Liu, C. E. Tracy, A. Mascarenhas, J. R. Pitts, S. K. Deb, *Solid State Ionics* **2003**, *165*, 111.
[43] K. R. Garrick Lim, A. D. Handoko, L. R. Johnson, Meng X, M. Lin, G. S. Subramanian, B. Anasori, Y. Gogotsi, A. Vojvodic, Z. W. She, *ACS Nano* **2020**, *14*, 16140.
[44] V. Briega-Martos, A. Ferre-Vilaplana, A. de la Peña, J. L. Segura, F. Zamora, J. M. Feliu, E. Herrero, *ACS Catal.* **2017**, *7*, 1015.
[45] G. Zhang, Q. Wei, X. Yang, A. C. Tavares, S. Sun, *Appl. Catal. B* **2017**, *206*, 115.
[46] L. Yu, X. Pan, X. Cao, P. Hu, X. Bao, *J. Catal.* **2011**, *282*, 183.
[47] M. H. Shao, P. Liu, R. R. Adzic, *J. Am. Chem. Soc.* **2006**, *128*, 7408.
[48] S. Gottesfeld, *Fuel Cell Catal. A Surf. Sci. Approach* **2008**, 1.
[49] S. Fletcher, *J. Solid State Electrochem.* **2009**, *13*, 537.
[50] S. Fajardo, P. Ocón, J. L. Rodríguez, E. Pastor, *J. Chem. Eng.* **2023**, *461*, 142053.
[51] G. Pérez, E. Pastor, C. F. Zinola, *Int. J. Hydrogen Energy* **2009**, *34*, 9523.
[52] C. F. Zinola, A. M. Castro Luna, W. E. Triaca, A. J. Arvia, *J. Appl. Electrochem.* **1994**, *24*, 119.

Manuscript received: November 15, 2023
Revised manuscript received: January 28, 2024
Version of record online: February 14, 2024

© 2024 The Authors. ChemElectroChem published by Wiley-VCH GmbH

21960216, 2024, 6, Downloaded from https://chemistry-europe.onlinelibrary.wiley.com/doi/10.1002/celc.202300673 by University Of Padova Center Di, Wiley Online Library on [04/02/2025]. See the Terms and Conditions (https://onlinelibrary.wiley.com/terms-and-conditions) on Wiley Online Library for rules of use; OA articles are governed by the applicable Creative Commons License